Available online at www.sciencedirect.com
SCIENCE DIRECT®
International Journal of Heat and Mass Transfer 48 (2005) 545–560
International Journal of HEAT and MASS TRANSFER
www.elsevier.com/locate/ijhmt

Flow structures and heat transfer of swirling jet impinging on a flat surface with micro-vibrations

Mao-Yu Wen *

Department of Mechanical Engineering, Cheng Shiu University, Kaohsiung 833, Taiwan, China

Received 13 November 2003; received in revised form 10 September 2004
Available online 6 November 2004

Abstract

This study focuses on the changes in the flow characteristics of a round jet issuing from a straight tube inserted with longitudinal swirling strips and impinging on a constant-heat-flux flat surface undergoing forced vibrations in the vertical plane. Smoke flow visualization is used to investigate the nature of the complicated flow phenomena under the swirling-flow jet for this impingement cooling. Effects of flow Reynolds number ($440 \leqslant Re \leqslant 27000$), the geometries of the nozzle (BR, LSS and CSS), jet-to-test plate placement ($3 \leqslant H/d \leqslant 16$), and surface vibration frequencies, f [0.3–10.19 Hz (the relative amplitude of the flat surface ranged from 0.5 to 8.1 mm)] are examined. In addition, correlations were developed to predict the Nusselt number for the vibration using the results of Wen and Jang [An impingement cooling on a flat surface by using circular jet with longitudinal swirling strips, Int. J. Heat Mass Transfer 46 (2003) 4657–4667] for the no-vibration case of the present study.

1. Introduction

Impingement has been, for a number of years, an accepted technique for cooling hot section components in industries ranging from textiles to electronic components. The effects of jet diameter, orientation, Reynolds number, and jet-surface spacing on flow and heat transfer on flat plates have been thoroughly investigated. Comprehensive reviews have been published by Jambunathan et al. [1] and Viskanta [2]. Impingement heat transfer studies by Ma [3] with meso-scale fluid jets revealed remarkable results. Hwang and Cheng [4] used the transient liquid crystal technique to investigate the swirl cooling characteristics in a triangular duct with an array of inclined jets impinging on a triangular apex. Recently, Swirl fluid flow and heat transfer characteristics in circular jets were examined in detail by Rose [5], Chigier and Chervinsky [6], and Zaman and Hussain [7,8]. Huang and El-Genk [9] obtained more uniform heat transfer effects on the impingement surface using multi-channel swirl generators and found that the heat transfer characteristics of impinging jet are affected by the nozzle shape and exit condition. Kataoka et al. [10] showed that the heat transfer on the impingement surface was greatly enhanced by large-scale intense eddy and vortex motion.

A comprehensive and widely cited review of correlations for impinging gas jets by Martin [11] did not include restrictions regarding the use of correlations with respect to the importance of surface motion. At a high rotational speed, a rotationally dominated flow pattern was observed near the disk surface and the influence of

* Tel./fax: +886 7 733 7100.
E-mail address: wmy@csu.edu.tw

0017-9310/$ - see front matter © 2004 Elsevier Ltd. All rights reserved.
doi:10.1016/j.ijheatmasstransfer.2004.09.010

Nomenclature

A	surface area of the test plate (m^2)
a	sectional area of the swirling-strip insert (m^2)
A_f	flow area of the tube = $(\pi d^2/4) - a$ (m^2)
A_m	surface vibration amplitude (mm)
b	thickness of the stainless steel foil (m)
d	inner diameter of the tube (m)
D_h	hydraulic diameter of the tube with swirling-strip insert = A_f/p (m)
f	surface vibration frequency (Hz)
H	jet-to-plate distance (m)
h	local convective heat transfer coefficient defined in Eq. (4) ($W\,m^{-2}\,K^{-1}$)
I	electrical current (A)
k	thermal conductivity of fluid ($W\,m^{-1}\,K^{-1}$)
k_s	thermal conductivity of the stainless steel foil ($W\,m^{-1}\,K^{-1}$)
L	length of the jet (m)
Nu	local Nusselt number defined in Eq. (5)
$\overline{Nu}$	average Nusselt number defined in Eq. (6)
Nu_o	Nusselt number at stagnation point
Pr	Prandtl number
p	the wetted perimeter (m)
q_g	generated heat flux ($W\,m^{-2}$)
q_{loss}	heat loss ($W\,m^{-2}$)
q_w	convective heat flux ($W\,m^{-2}$)
Re	jet Reynolds number, $4\dot{V}/\pi v D_h$
T_{aw}	adiabatic wall temperature (K)
T_i	temperature at the inner bed of the heater (K)
T_j	air temperature at the jet exit (K)
T_j^*	heated jet temperature (K)
T_w	wall temperature (K)
u	average velocity of air in the jet = $\frac{\dot{V}}{A_f}$ ($m\,s^{-1}$)
V	voltage drop across the surface (V)
$\dot{V}$	volumetric flow rate = uA_f ($m^3\,s^{-1}$)
r	radial distance from the stagnation point (m)
z	axial length of the tube (m)

Greek symbols

δ	strip thickness (m)
$\cos\phi$	power factor
v	kinematic viscosity of air ($m^2\,s^{-1}$)
ρ	density ($kg\,m^{-3}$)

Subscripts

BR	tube without any insert
CSS	crossed-swirling-strip insert
f	with vibration
LSS	longitudinal swirling-strip insert
n	without vibration

the impinging jet flow on heat transfer was reduced [12,13]). Results indicated that the impinging jet flow could become severely disrupted due to the entrainment of surrounding air by the rotational motion of the disk. In addition, Martin [11] also considered, only when the impinging flow is not disrupted by the motion imparted to the surrounding fluid. It should be noted that the flow disruption of a submerged jet by the fluid entrained by a surface motion demonstrates the importance of surface motion in affecting heat or mass transfer rates. However, when the jet flow and plate motion are opposed, the fluid is entrained and it re-enters the impingement region. As a result of the complicated relationship between the impinging flow and motion plate, the flow velocity profiles are significantly affected, which, in turn, influence the convection heat transfer.

Most of the above studies of jet impingement cooling mainly focused on a circular tube without/with either decaying or continuous swirling flow on a flat plate. The impingement cooling on a flat surface by using a jet issuing through the longitudinal swirling strips has not been performed. In a typical package, heat dissipation elements are often with the vibration surface since many electronics circuits are designed to produce higher levels of heat dissipation per unit of component surface area. In addition, chilled tower (air-cooled type) equipped with a mini vibrating motor is a cooling device combined with the vibrating surface. However, heat and fluid flow, which are employed by engineers to develop specifications for jet cooling or drying systems, rarely account for surface vibration effects. The behavior of the swirling impinging jet on the vibrating surface is not well known because most of the investigations were focused on impulsively started gas jets.

This work is a continuation of our previous study regarding the heat transfer between the constant-heat-flux test plate and the impinging jet with longitudinal swirling strips [14]. Smoke flow visualization was used to investigate the behavior of the complicated flow phenomena, and the effects of swirling-flow Reynolds numbers, the geometry of the nozzle (BR, LSS and CSS), and jet-to-test plate placement were examined. Correlations of the stagnation point Nusselt number (Nu_o) as well as the average Nusselt number ($\overline{Nu}$) had been derived for all types of nozzles and other pertinent variables.

The focus of the previous investigation was on the heat transfer between the stationary test plate and the impinging jet with longitudinal swirling strips. In this

Table 1
The surface oscillation frequencies and the relative amplitudes of the flat surface

Surface oscillation frequencies, f (Hz)	The relative amplitudes of the flat surface, A_m (mm)
0	0
0.30, 1.15, 2.53, 5.02, 6.67, 10.19	0.5
0.30, 1.15, 2.53, 5.02, 6.67, 10.19	1.3
0.30, 1.15, 2.53, 5.02, 6.67, 10.19	2.5
0.30, 1.15, 2.53, 5.02, 6.67, 10.19	3.6
0.30, 1.15, 2.53, 5.02, 6.67, 10.19	6.3
0.30, 1.15, 2.53, 5.02, 6.67, 10.19	8.1

paper, the heat transfer between the vibrating test plate and the impinging jet with longitudinal swirling strips will be developed. With the swirling flow and vibrating plate, the flow structures of the impinging jets will be changed, and the heat transfer characteristics of impingement plate will also be affected by the change in flow structures. This study focuses on the changes in flow and heat transfer characteristics of swirling impinging on a plate generated with the micro-vibrations. The effects of different nozzle types, Reynolds number, nozzle-to-surface spacing and surface oscillation frequencies on the flow behavior and the heat transfer are analyzed. An experiment is conducted using different tube Reynolds numbers (440–27 000) for jet exit-to-surface spacing from 3 to 16 tube diameter and the surface vibration frequencies in the range of 0.3–10.19 Hz (the relative amplitude of the flat surface was in the range of 0.5–8.1 mm) (see Table 1). In addition, flow visualization is employed to observe the jet vortex structure during impingement on the flat surface undergoing forced vibrations along the longitudinal plane. For completeness and contrast, visualization of a free jet and a jet impinging on a flat surface are also presented.

2. Experimental setup

2.1. Experimental apparatus

A schematic representation of the test setup is shown in Fig. 1. Air supply from a blower system passes through a heat exchanger, a shut-off valve, a filter, a flow meter and a settling chamber before entering the circular tube. The tube was made of copper. It had an internal diameter of 7 mm, a wall thickness of 1.0 mm, and a length of 250 mm. In addition, in order to impart swirl to the jet, the tube had different longitudinal swirling strip inserts as shown in Fig. 2. The swirling strip was made of 1.5 mm thick copper strips, the width of the strip being 0.1 mm more than the inside diameter of the tube. The strips were twisted on a lathe by the manual rotation of the chuck. There was interference fit between the tube and the swirling strip insert. The total air flow rate was controlled by an inverter. A heat exchanger was installed to obtain a constant temperature flow at the nozzle exit and to reduce the temperature difference between the ambient air and the air nozzle exit within ±0.2 °C. A uniform and stable flow distribution was established at the tube exit using a settling chamber of $450 \times 450 \times 500$ mm^3 in volume. Air rotameters were used to measure the air volumetric flow rate ($\dot{V}$) (it is measured by one of the three flow meters depending on the range), which was corrected using the measured air temperature and pressure after exiting the flow meters. The jet support frame was used to adjust the elevation, H of the jet from the heated surface and to maintain the jet in the vertical position.

A DC servomotor powered the drive shaft (its height can be adjusted) carrying the two different, rotating bodies at each end as shown in Fig. 1. The flat surface undergoes forced vibrations in the vertical plane. With this system, the oscillation frequency of the plate, f, could be set in the range of 0.3–10.19 Hz. This placement profile of the oscillating plate was measured by tracking the motion of the plate using an electro-optical displacement follower (accelerometer). This was done in order to assess the accuracy of the drive system in providing sinusoidal motion to the cylinder. The resulting time traces indicated that there was some dwell at the end of the stroke for low oscillation frequencies, ranging from 0.1 to 0.4 Hz. However, this dwell became negligible at higher oscillation frequencies. The inaccuracy during measurements was deemed sufficiently small, while the motion of the cylinder was adequately sinusoidal for our purposes, over the desired range of vibration frequencies. From the time traces, we have the surface vibration frequencies in the range of 0.3–10.19 Hz and the relative amplitudes of vibration of the flat surface ranged from 0.5–8.1 mm.

2.2. Data reduction and uncertainty

The heat flux, q_g in the heating foil was controlled by varying the output voltage, and this was calculated by measuring the voltage drop (V) between the voltage taps soldered on to the heating foil, the electrical current (I) and the power factor ($\cos\phi$). The convective heat flux (q_w) can be calculated as

$$q_w = q_g - q_{loss} \approx \frac{VI\cos\phi}{A}, \quad (1)$$

where A is the area of the test plate (heated foil). The term q_{loss} is a small correction for conduction and radiation losses from the element. The correction never exceeded 3% of q_g in the present study. By performing a detailed analysis, the maximum possible errors are

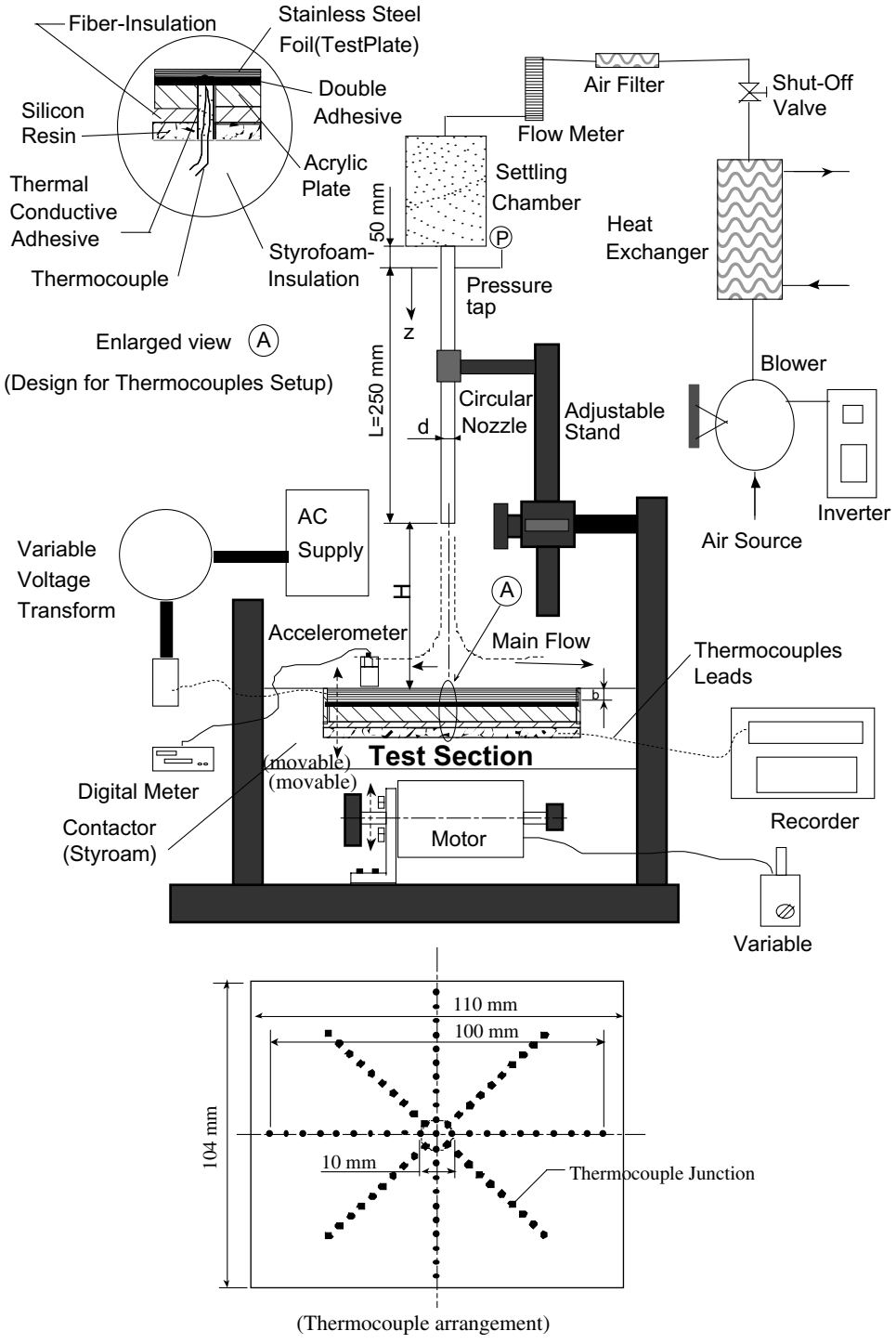

Fig. 1. A schematic of the experimental setup and thermocouple arrangement.

individually obtained as follows: (1) radiation loss: 0.1%, (2) non-uniformity of the heating foil: 1.8%, (3) lateral solid heat conduction: 0.5%, and (4) heat loss through insulation: 0.4%. The wall temperature T_w at the outer surface of the heater can be calculated by the one-dimensional heat conduction model at each applied heat flux (q_w) as

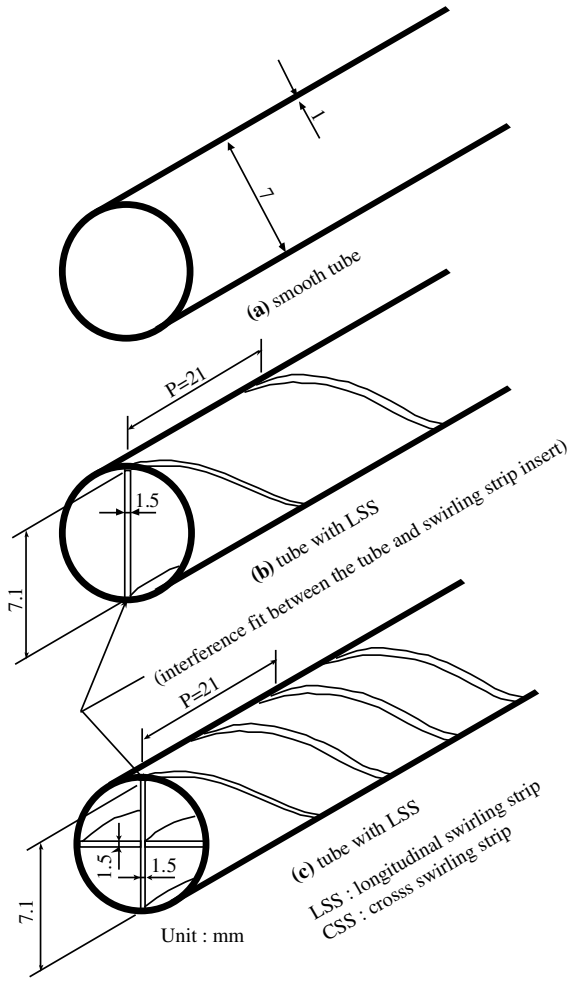

Fig. 2. Experimental apparatus for nozzle geometry.

$$T_w = T_i - \frac{q_w b}{k_s}. \quad (2)$$

The Reynolds number is defined as $Re = uD_h/v$ where u is the velocity of air leaving the tube, D_h is the hydraulic diameter, and v is the kinematic viscosity of air. Putting $\dot{V} = uA_f$, we have

$$Re = 4\dot{V}/\pi v D_h. \quad (3)$$

The effects of jet entrainment temperature on heat transfer have been investigated by Striegl and Diller [15], Hollworth and Gero [16], Goldstein et al. [17], and Baughn et al. [18]. The heat transfer coefficient is defined in terms of the difference between the heated wall temperature and the adiabatic wall temperature and it is independent of the temperature difference between the jet and the ambient. Therefore, it is possible to use the heat transfer data for an unheated jet ($T_j^* = T_j$) for the heated jet if the effectiveness is known and the local heat transfer coefficient is defined in terms of the adiabatic wall temperature. The local heat transfer coefficient based on the difference between the wall temperature and adiabatic wall temperature is well established [19,20]. The local heat transfer coefficient is defined as

$$h = \frac{q_w}{T_w - T_{aw}}, \quad (4)$$

the adiabatic wall temperature ($T_{aw} = T_i$) distribution is measured at the inner surface of test plate based on zero wall-heat flux. Approximately 0.5 h is required to reach steady-state condition for each test run. Experimental results for heat transfer are presented in terms of the Nusselt number

$$Nu = \frac{hD_h}{k}. \quad (5)$$

The uncertainty analysis was performed by using the methods suggested by Kline and McClintock [21] with 95% confidence level. The maximum measurement uncertainties are: Heat flux ±1.7%; Heat transfer coefficient ±6.2%; Nusselt number ±6.5%; Reynolds number ±3.0%; Dimensionless parameter (fA_m/u) ±3.2%.

3. Results and discussion

Three cases with a jet impinging normal to the vibrating surface were considered. One case had an open tube (BR), the other had a longitudinal swirling strip insert (LSS), and the last one had a cross swirling strip insert (CSS). The experiments were conducted at ten different Reynolds numbers (440, 500, 750, 1000, 2100, 4400, 9300, 16 500, 21 000 and 27 000) and the surface vibration frequencies, f (0.3–10.19 Hz (the relative amplitude of the flat surface are ranged of 0.5–8.1 mm) for jet-to-plate spacings (H/d) of 3, 5, 8, 12 and 16).

3.1. Flow visualization

The smoke from a smoke generator is injected into the plenum before the blower is turned on. The flow visualization experiments were conducted using both the strong-full light resource and the plane of light, a black background, a camcorder and a 35 mm camera to record images of the flow fields. The smoke flow technique was used to show images of the complete flow field, both between the jet exit and impinged surface with micro-vibrations, and horizontally along the impinged surface, up to 35 mm from stagnation point.

Fig. 3(A)—(a), (c) and (e) shows the visual images of impingement on the stationary plate for BR, LSS, and CSS at $Re = 440$ and $H/d = 3$. In general, the impinging flow structures before arriving at the wall observed for the round jet with LSS/CSS are significantly different from that of the round jet without any insert. The flow

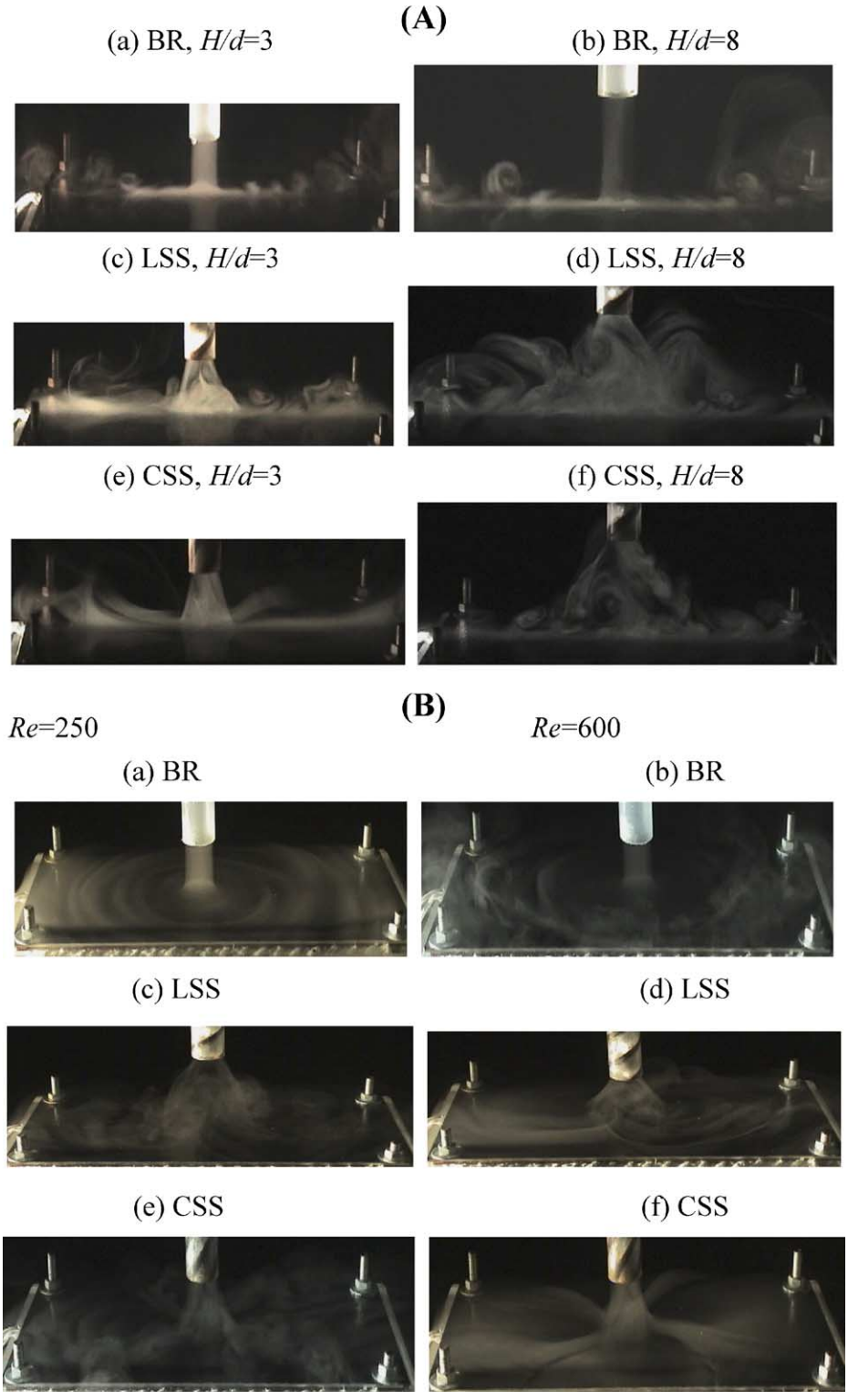

Fig. 3. Visualized images of impingement on the stationary plate for different nozzle types: (A) jet-to-plate distances at Re = 440, and (B) Reynolds number at H/d = 3.

fields of CSS (Fig. 3(A)—(e)) showed four distinct radial flow streams in the housing tube and extending to about 1.5 jet diameter from the jet exit before combining to form a flow cone similar to that of BR (Fig. 3(A)—(a)), but with a larger diameter at the top due to higher entrainment of ambient air (Fig. 3(A)—(c) and (e)). In addition, Fig. 3(A)—(b), (d) and (f) displayed the flow fields of BR, LSS and CSS at $Re = 440$ and $H/d = 8$. Similar to the flow structures shown in Fig. 3(A) (left), the radial spread of the air jet on the impinged surface decreased upon increasing the jet-to-plate spacing. Fig. 3(B) shows photographs of the entire flow field of impingement on a stationary surface for different nozzle types and Reynolds number at $H/d = 3$. When the Reynolds number is increased, these vortices moved radially outward and the mixing occurring at the stagnation point by CSS (Fig. 3(B)—(f)) was also more efficient than by LSS (Fig. 3(B)—(d)) and BR (Fig. 3(B)—(b)).

Fig. 4 shows the visualized images of impinging on a vibrating surface for different nozzle types and jet-to-plate distance at $Re = 440$ and $f = 2.53$ Hz (the relative amplitude is 1.3 mm) through (A) a strong-full light resource and (B) a plane of light. First, considering the vibration effects at a spacing of $H/d = 3$ and $Re = 440$, a transition from laminar (Fig. 4 (left)) to unsteady flow along the surface is observed at a lower vibration frequency *of* 2.53 Hz. When the plate was at the oscillation frequency of $f = 2.53$ Hz, the shear layers developed abrupt instabilities in the form of annulus vortices, and such vortices could be rolled up, and induced by the plate acceleration along the vertical direction. Therefore, visualization of vortices shed from the vibrating plate was not as good as that of the stationary plate. Furthermore, when the vibration frequency is increased, the flow along the surface is unsteady and vortices can be observed on the surface, even though they break down rapidly. In addition, in order to express more effectively, the illumination of the smoke through a plane of light is preformed as displayed in Fig. 4(B). The situation shown in Fig. 4(B) are similar to those shown in Fig. 4(A). When the spacing of H/d is increased, the axial/radial oscillation of the surface flow is also increased.

The flow field for the present BR, extending from the exit of the jet housing tube to impinged surface with the micro-vibration can be divided into six characteristic regions as shown in Fig. 5(a). They are (1) free jet; (2) impinged area; (3) cross flow; (4) flow separation; (5) entrainment; (6) axial/radial oscillations of surface flow. This methodology is consistent with those of other studies that examined the characteristic regions (but a slight difference was obvious as shown in Fig. 5)) including Huang and El-Genk [9], and Shlien and Hussain [22].

Before impinging the surface, the air exiting the jet housing tube in the present experiments was a free jet (region 1). The free jet was turbulent but not fully developed as it impinged the surface. Just below the free jet flow region, resided the impinged area region (region 2). The impinged area in the vicinity of the stagnation point had a diameter of $\sim$1.5–3.0d, depending on jet-to-plate placement and Reynolds number. When impinging the surface, most part of the flow kinetic energy was converted into a static pressure, forcing the air to flow in a boundary layer along the impinged surface (region 3).

The cross flow region decelerated quickly upon increasing the radial distance from the stagnation point due to the increase in the flow cross-sectional area and the entrainment of surrounding air. As the boundary layer flow became laminar and thicker with increased radial distance from the stagnation point, the flow kinetic energy became too low to sustain radial flow. Subsequently, the combination effects of radial laminar flow and entrainment of surrounding air (region 5) caused the formation of vortices at some distance from the stagnation point (region 4). In addition, vortex formation from the shear layers is modified by the plate acceleration when the plate is forced to vibrate (region 6). This modification process caused by the plate acceleration is synchronized with the outward radial movement of the vortex. The flow field for the present LSS (Fig. 5(b)) was distinctly different from that of BR as shown in Fig. 5(a). After the flow exiting the jet housing tube, it formed a swirling, cone-shaped flow field. The spiral effect stimulated more entrainment of the surrounding air than BR at the same conditions. In addition, the impinged area (region 2) of LSS was significantly larger than that of the BR at the same conditions. The flow field of LSS on the impinged area was shaped like a donut (region 7). The flow mixing in the central zone of the donut region was effective, but less strong than that in the donut region, resulting in a relatively higher heat transfer rate at the stagnation point than BR. The spiral flow outside the donut region spread the air flow field radially outward, along the impinged surface, and the induced convection resulted in higher heat transfer rate than for BR. The flow model developed for CSS in Fig. 5(c) is basically the same as that for LSS, except that the flow developed into four radial components by CSS (Fig. 5(c)) differ from the two radial components by LSS. Such enhancement in heat transfer outside the donut region was responsible for the improved radial uniformity of $Nu(r)$ by CSS.

3.2. Heat transfer coefficient

Effects of the vibration frequency, f, and the amplitude, A_m on the stagnation point Nusselt number, Nu_o, are presented in Fig. 6. The figure shows plots of Nu_o versus vibration frequency with the relative amplitude, $A_m = 3.6$ mm, at $H/d = 3$ and $Re = 16\,500$ for three

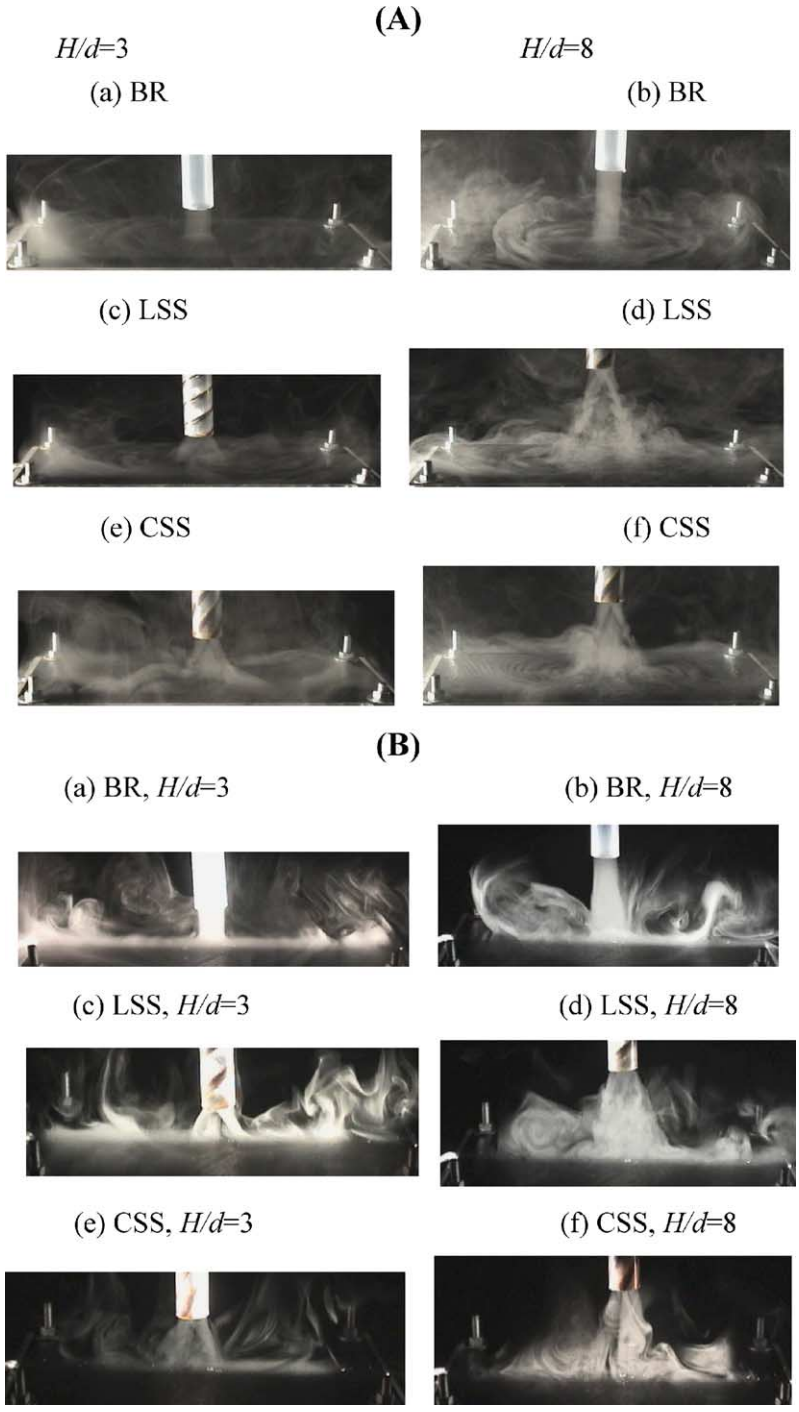

Fig. 4. Visualized images of impingement on a vibrating surface for different nozzle types and jet-to-plate distances at $Re = 440$ and $f = 2.53$ Hz (the relative amplitude is 1.3 mm) through (A) a strong-full light resource, and (B) a plane of light.

different nozzle types. For any nozzle type, we note that Nu_o increases with the vibrational excitement, in comparison to the case without any vibrations. The waves generated by the vibrating device are reflected at the top of the plate. These reflected waves make the air film roll-up, resulting in a forced convective region which is characterized by this air film with heat transfer by convection and conduction at the solid-air interface. Conse-

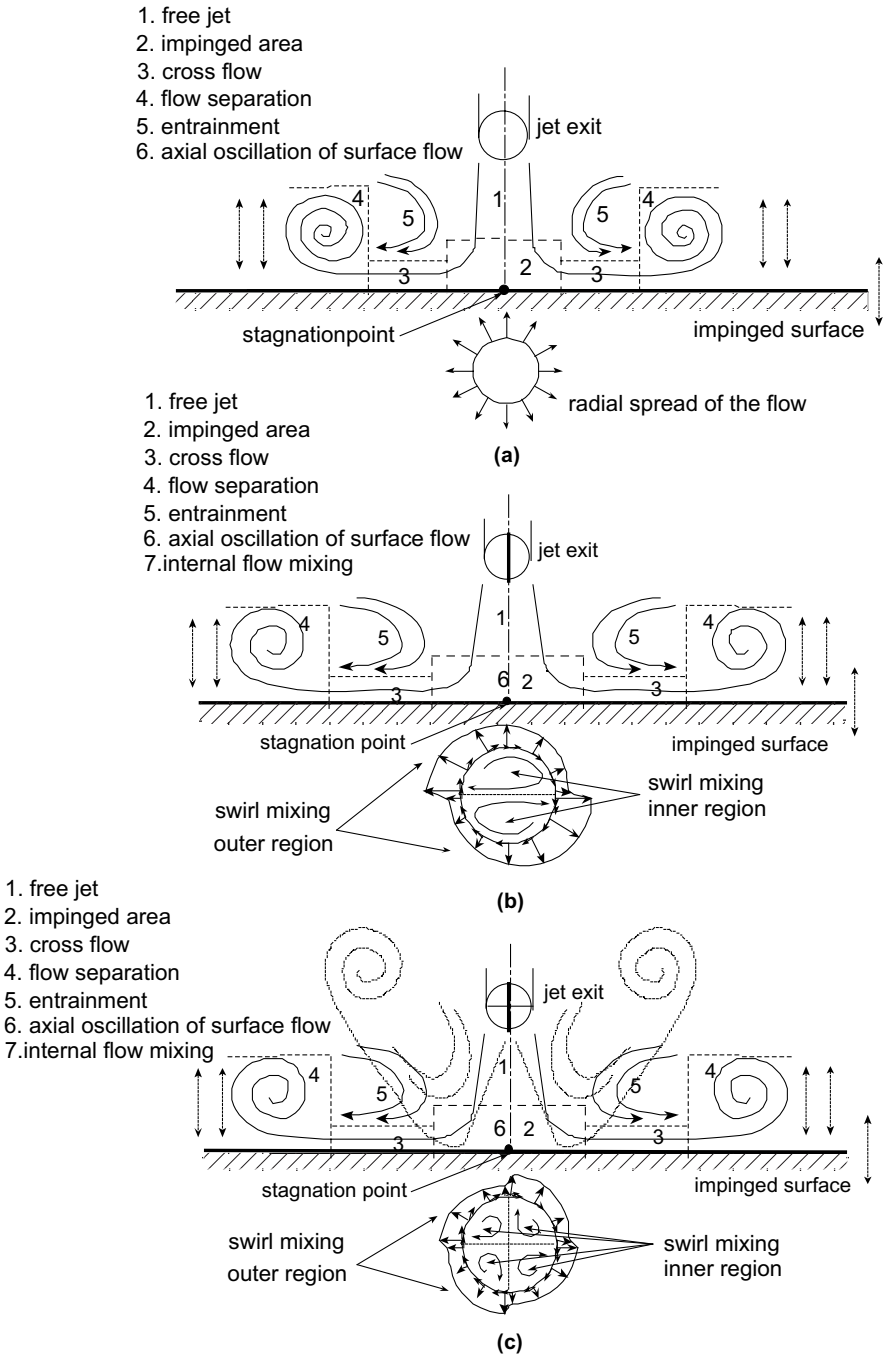

Fig. 5. The flow model developed for BR, LSS and CSS based visual observations of impingement on the vibrating plate.

quently, the heat transfer coefficient increases. From Fig. 6(b) we also observe that for a given vibration frequency ($f = 5.02$ Hz), Nu_o increases with increasing the amplitude of vibration. The results also show that the improvement in Nu_o as compared to the no-vibration case, is only about 3–4% for both Fig. 6(a) and (b). This is presumably because that the impinging air pressed the vortex formation from the shear layers to be rolled up, induced by the plate acceleration in the vertical direction.

Using numerical integration, the average Nusselt number ($\overline{Nu}$) is given by Eq. (6) as follows:

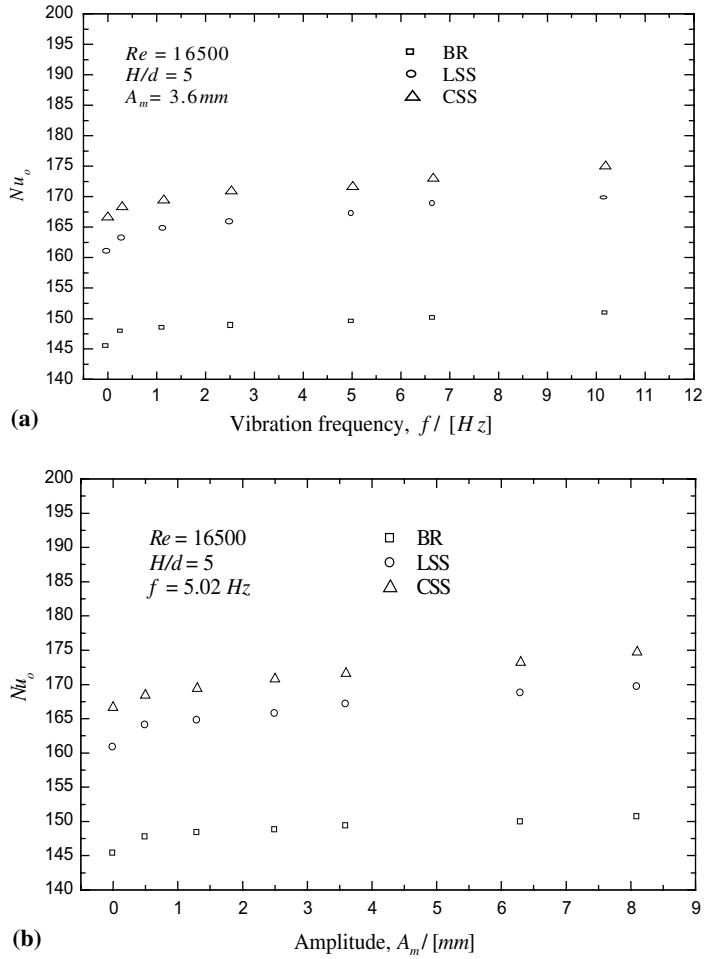

Fig. 6. Stagnation point Nusselt number as function of (a) the vibration frequency and (b) the amplitude for different nozzle types.

$$\overline{Nu} = \frac{2}{r^2}\int_0^r r \cdot Nu \cdot \mathrm{d}r. \tag{6}$$

In Fig. 7, the average Nusselt number, $\overline{Nu}$, for different vibration frequency and vibration amplitude are illustrated at the conditions of the nozzle-to-plate distance ($H/d = 5$) and the Reynolds number ($Re = 16\,500$). As expected, a significant increase of $\overline{Nu}$ upon increasing f and A_m for these three nozzle types (BR, LSS and CSS) were found to be similar to those for Nu_o as shown in Fig. 6. However, the $\overline{Nu}$ values are 1.12-fold greater as compared with those for vibrationless cases. These results tend to suggest that at higher vibration frequencies/amplitudes, the interface between the solid and the air becomes more-turbulent (see Fig. 4), which result in an increase in the specific interfacial area resulting in better gas–solid contact and better heat transfer. The waves generated by the vibrating device are reflected at the top of the plate. These reflected waves lead to cool air film hold-up, resulting in a forced convective region which is characterized by the air film with convection and conduction heat transfer at the solid–air interface. Consequently, the heat transfer coefficient is increased.

The local Nusselt number distribution along the plate without/with the vibration (for $f = 5.02$ Hz and $A_m = 3.6$ mm) is shown in Fig. 8 for different nozzle types (BR, LSS and CSS) with $Re = 16\,500$ and $H/d = 5$. Similar to the results obtained for the vibrationless cases, Nu decreased with increasing the radial distance from its maximum value at (for BR) and near (for LSS and CSS) the stagnation point. Furthermore, this result clearly demonstrated that both the LSS and CSS markedly enhanced the heat transfer rate on the impinged surface with the micro-shock vibration having the same Re and H/d compared to that of BR. However, Nu values for the CSS were much higher than those for LSS and BR, particularly at and near the stagnation point. It was found that Nu in the vibration cases at each radial distances for all the different nozzles, compared to

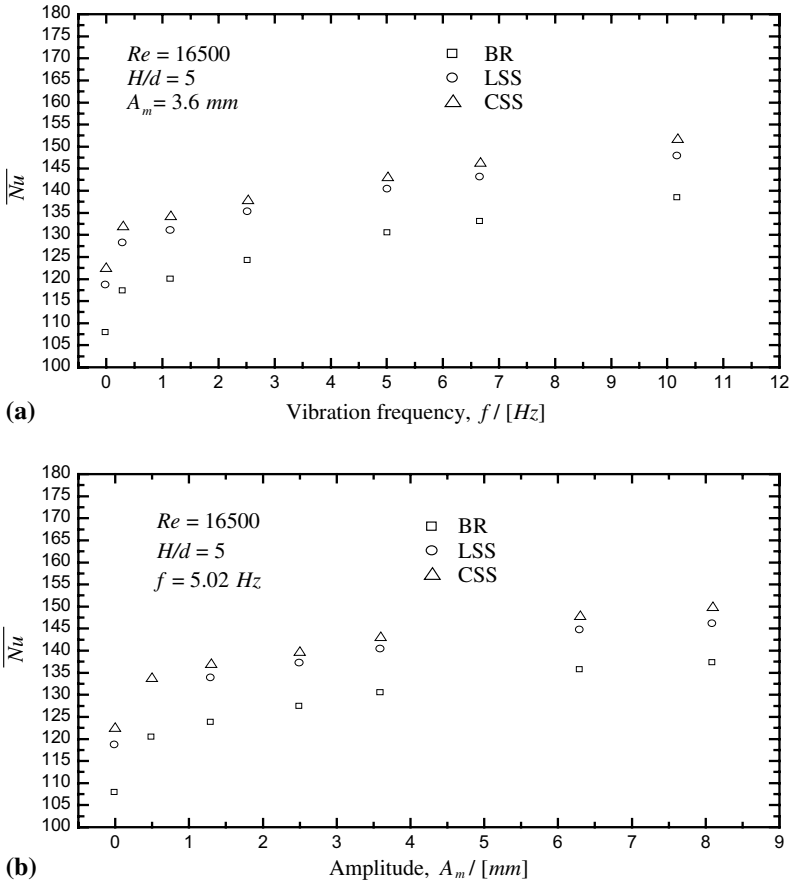

Fig. 7. The average Nusselt number as a function of (a) the vibration frequency and (b) the amplitude for different nozzle types.

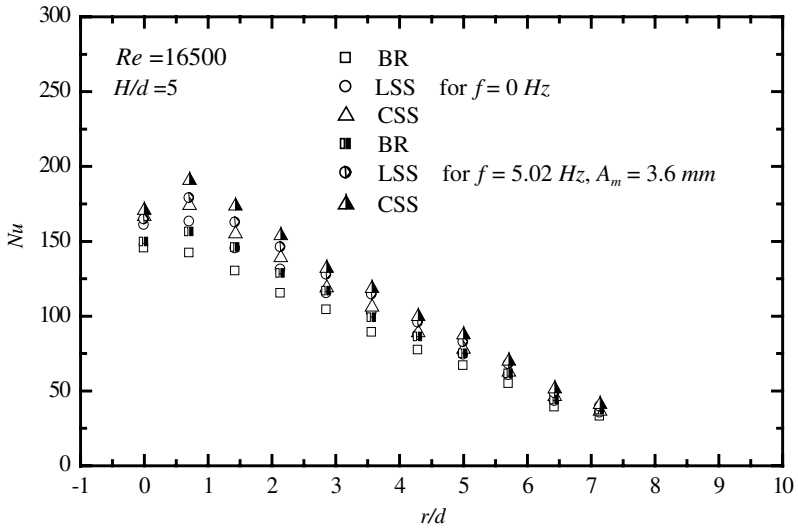

Fig. 8. Measured radial Nusselt number distribution on stationary/vibrating surface and at $H/d = 5$, $Re = 16\,500$, $f = 0/f = 5.02$ Hz ($A_m = 3.6$ mm).

that of the no-vibration cases, had an average increase of about 12.2%. It also implied that no perceptible dependence of Nu on r/d for the present vibration cases was detected.

Fig. 9(a) and (b) shows the stagnation point Nusselt number (Nu_o) and the average Nusselt number ($\overline{Nu}$) in the present plate without/with the vibration cases versus nozzle-to-plate distance (H/d) for three different nozzles, respectively. In general, Nu_o and $\overline{Nu}$ data show the same dependence (the trend) on H/d as observed in the no-vibration cases. The Nu_o and $\overline{Nu}$ in the vibration cases at each H/d for all the different nozzles, compared to that of the vibrationless cases, had the average increase of about 3.8% and 12.3%, respectively. We could not find any perceptible dependence of $(Nu_{o,f} - Nu_{o,n})$ on H/d.

Considering the effects of different nozzles on the stagnation point Nusselt number (Nu_o) and the average

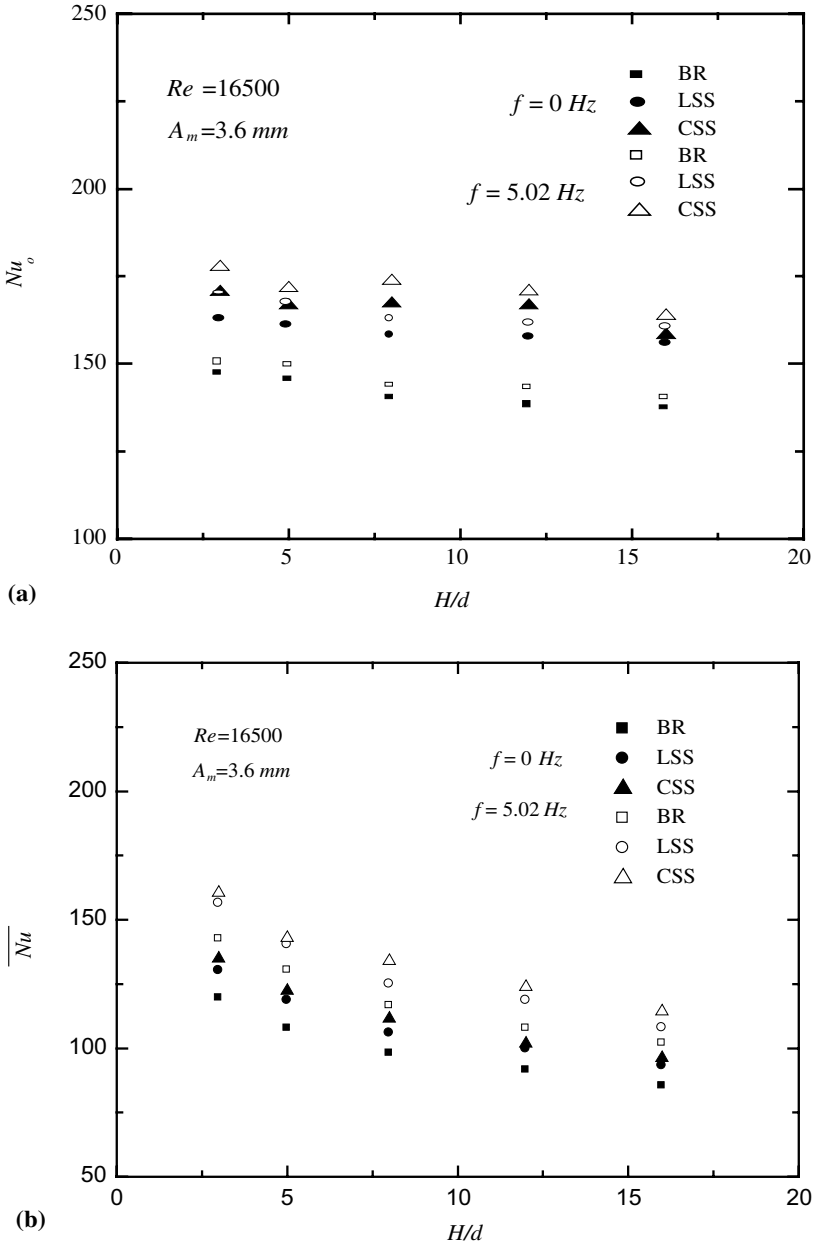

Fig. 9. (a) Stagnation point Nusselt number, (b) the average Nusselt number vs. H/d for different nozzles.

Nusselt number ($\overline{Nu}$) in the present plate without/with the vibration cases with respect to Reynolds number, both Nu_o and $\overline{Nu}$ are plotted against the Reynolds number as shown in Fig. 10(A) and (B), respectively.

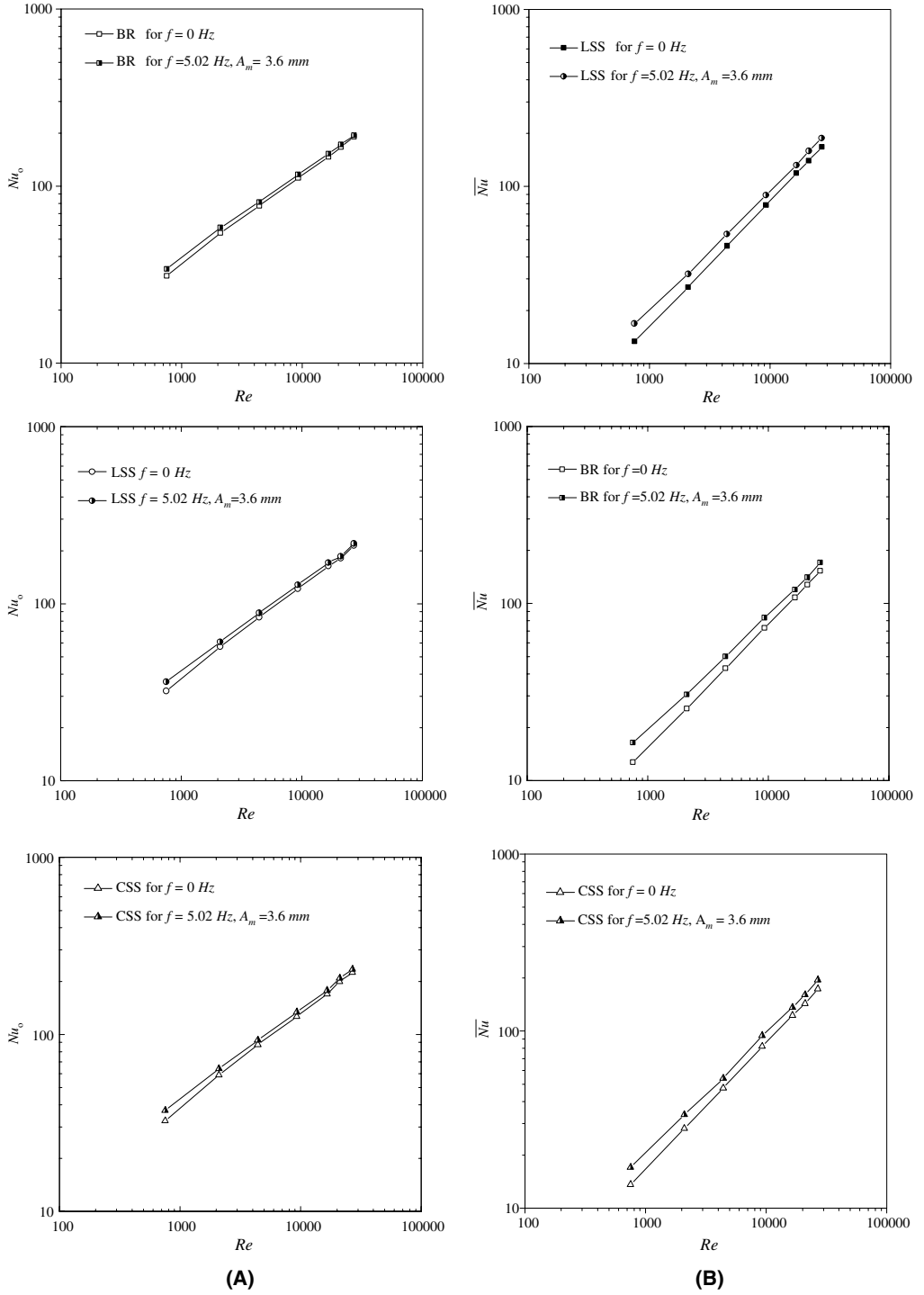

Fig. 10. Variation of (A) the stagnation point number, (B) the average Nusselt number with Reynolds number for different nozzles on stationary/vibrating surface and at $H/d = 5$, $f = 0/f = 5.02$ Hz ($A_m = 3.6$ mm).

Both Nu_o and $\overline{Nu}$ data for the vibration cases show the same dependence (the trend) on Re as does the no-vibration cases, but the differences between $(Nu_{o,f} - Nu_{o,n})$ and $(\overline{Nu}_f - \overline{Nu}_n)$ decrease gradually as the Re increases.

3.3. Correlations of Nusselt number

Both Nu_o and $\overline{Nu}$ for the no-vibration cases in the present study had been correlated [14]. In this paper we have mainly demonstrated that significant improvement in heat transfer coefficient could be realized by vibrational excitation. The effects of H/d on the stagnation point Nusselt number and the average Nusselt number in the present study with the vibrating plate shown in Fig. 9(a) and (b) seems insignificant (the variation of $(Nu_{o,f} - Nu_{o,n})$ and $(\overline{Nu}_f - \overline{Nu}_n)$ vs. H/d are all less than 1%). However, it was found that both the $(Nu_{o,f} - Nu_{o,n})$ and $(\overline{Nu}_f - \overline{Nu}_n)$ increase mainly due to the increase in f (see Fig. 6(A) and (B)), A_m (see Fig. 7(A) and (B)), and Re (see Fig. 10(A) and (B)). This indicates that the correlations of the stagnation Nusselt number $(Nu_{o,f} - Nu_{o,n})$ and the average Nusselt number $(\overline{Nu}_f - \overline{Nu}_n)$ vs. the dimensionless parameter (fA_m/u) involving the vibrational frequency (f), vibrational amplitude (A_m) and the average velocity of air in the jet (u) for different nozzles will be like the plots in Figs. 11 and 12. The value of (fA_m/u) implied in this way will be different from the classical Strouhal number. We now return to the literature to examine the results in the context of Strouhal numbers and impinging jets. Recent papers by Ho and Nosseir [23] and by Ziada [24] illustrate the mechanism of excitation very clearly. Two scaling approaches have been used for the impinging jet frequency. Both of them center on the Strouhal number. The Strouhal number St indicates the frequency characteristics of the flow and is defined by

$$St = \frac{fL_c}{V_c}, \tag{7}$$

where L_c and V_c are characteristic length and velocity scales, and f is the frequency. The jet velocity at the origin, u, for the present study is the clear choice for V_c, provided the jet is round or planar. The choice of L_c is H at a fixed value of d, as the length scale impact the frequency. Similarly, the vibration amplitudes (A_m) of the plate from the vibration exciter in the present study is the choice of L_c. These findings strongly suggest that the underlying mechanism for the present impingement on a surface with micro-vibrations can be expressed like the plots in Figs. 11 and 12 for the correlations of stagnation Nusselt number $(Nu_{o,f} - Nu_{o,n})$ and the average Nusselt number $(\overline{Nu}_f - \overline{Nu}_n)$ vs. (fA_m/u) for different nozzles. The correlation predicts 98% of points within ±20% and 85% of points within ±10%. The results are satisfactorily correlated as

$$Nu_{o,f} = Nu_{o,n} + 5.40(fA_m/u)^{0.25} \quad \text{for present BR}, \tag{8}$$

$$Nu_{o,f} = Nu_{o,n} + 8.97(fA_m/u)^{0.39} \quad \text{for present LSS}, \tag{9}$$

$$Nu_{o,f} = Nu_{o,n} + 8.37(fA_m/u)^{0.44} \quad \text{for present CSS} \tag{10}$$

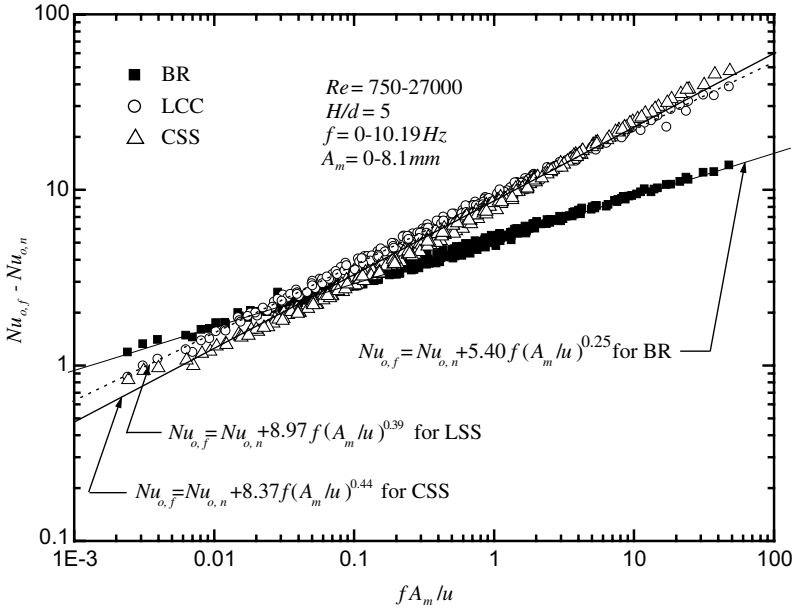

Fig. 11. The difference between $Nu_{o,f}$ and $Nu_{o,n}$ vs. the dimensionless parameter $(fA_m u)$ for different nozzle types.

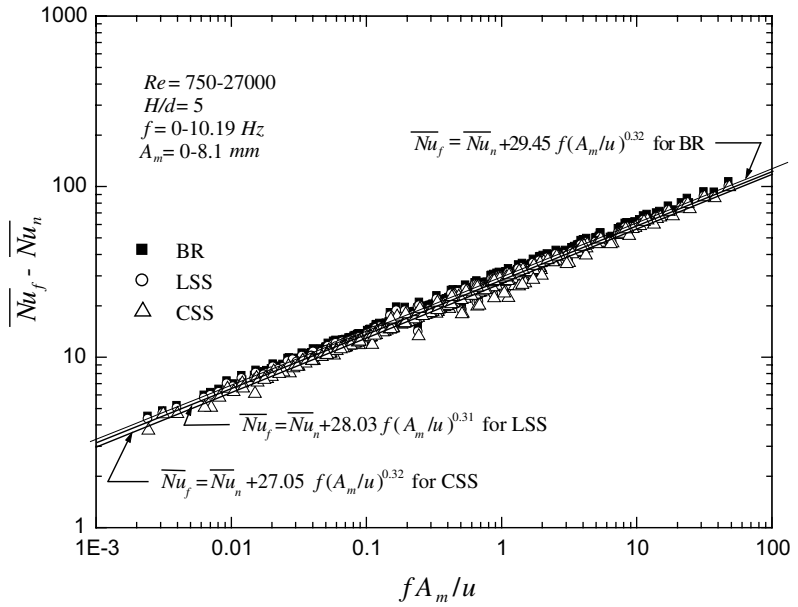

Fig. 12. The difference between $\overline{Nu}_f$ and $\overline{Nu}_n$ vs. the dimensionless parameter (fA_mu) for different nozzle types.

and

$$\overline{Nu}_f = \overline{Nu}_n + 29.45(fA_m/u)^{0.32} \quad \text{for present BR,} \qquad (11)$$

$$\overline{Nu}_f = \overline{Nu}_n + 28.03(fA_m/u)^{0.31} \quad \text{for present LSS,} \qquad (12)$$

$$\overline{Nu}_f = \overline{Nu}_n + 27.05(fA_m/u)^{0.32} \quad \text{for present CSS} \qquad (13)$$

in the range $3 \leqslant H/d \leqslant 16$, $0 \leqslant r/d \leqslant 7.14$ and $440 \leqslant Re \leqslant 27000$. The maximum deviation of the above correlations and the average Nusselt numbers obtained from the experimental data is less than ±10%.

4. Conclusions

Flow visualization experiments were performed to investigate and compare the flow structures of the swirling jets (LSS and CSS) with that of a conventional impinging jet (BR) having the same tube diameter and conditions. The experiments were performed using a fixed jet diameter (d = 7 mm) and the test plate (stainless steel foil). The Reynolds number was varied from 440 to 27000, and the jet-to-plate distance was also varied in the range of 3–16. The surface oscillation frequencies, f [0.3–10.19 Hz (the relative amplitude of the flat surface are ranged of 0.5–8.1 mm)] are also examined. The major conclusions are listed in the following:

1. The variations of $(Nu_{o,f} - Nu_{o,n})$ and $(\overline{Nu}_f - \overline{Nu}_n)$ in the present study with the vibrating plate were strong functions of f, A_m and Re, but no perceptible dependence of $(Nu_{o,f} - Nu_{o,n})$ and $(\overline{Nu}_f - \overline{Nu}_n)$ on H/d was detected.
2. The correlations (8)–(13) could be used to predict the stagnation point Nusselt number (Nu_o) as well as the average Nusselt number ($\overline{Nu}$) for the present swirling jet impinging on the vibrating plate in the range $3 \leqslant H/d \leqslant 16$, $0 \leqslant r/d \leqslant 7.14$, $440 \leqslant Re \leqslant 27000$, $0.3 \leqslant f \leqslant 10.19$ Hz and $0.5 \leqslant A_m \leqslant 8.1$ mm by using the results of Wen and Jang [14] for the present swirling jet impinging on the no-vibration plate.

References

[1] K. Jambunathan, E. Lai, M.A. Moss, B.L. Button, A review of heat transfer data for singular jet impingement, Int. J. Heat Fluid Flow 13 (1992) 106–115.
[2] R. Viskanta, Heat transfer to impinging isothermal gas and flame jets, Exp. Thermal Fluid Sci. 6 (1993) 111–134.
[3] C.F. Ma, Impingement heat transfer with meso-scale fluid jets, in: Proceedings of 12th International Heat Transfer Conference, 2002.
[4] J.J. Hwang, T.S. Cheng, Augmented heat transfer in a triangular duct by using multiple swirling jets, ASME J. Heat Transfer 121 (1999) 683–690.
[5] W.G. Rose, A swirling round turbulent jet 1—mean-flow measurements, J. Appl. Mech. 29 (1962) 615–625.
[6] N.A. Chigier, A. Chervinsky, Experimental investigation of swirling vortex motions in jets, J. Appl. Mech. 89 (1967) 443–451.
[7] K.B.M. Zaman, A.K.M.F. Hussain, Vortex pairing in a circular jet under controlled excitation, Part 1. General jet response, J. Fluid Mech. 101 (1980) 449–491.

[8] K.B.M. Zaman, A.K.M.F. Hussain, Vortex pairing in a circular jet under controlled excitation, Part 2. Coherent structure dynamics, J. Fluid Mech. 101 (1980) 493–544.
[9] L. Huang, M.S. El-Genk, Heat transfer and flow visualization experiments of swirling, multi-channel and conventional impinging jets, Int. J. Heat Mass Transfer 41 (1980) 583–600.
[10] K. Kataoka, L. Mihata, K. Maruo, M. Suguro, T. Chiguesa, Quasi-periodic large-scale structure responsible for the selective enhancement of impinging jet heat transfer, in: Proceedings 8th IHTC 3, 1986, pp. 1193–1198.
[11] H. Martin, Heat and mass transfer between impinging gas jets and solid surfacesAdvances in Heat Transfer, vol. 13, Academic Press, New York, 1977, pp. 1–60.
[12] D.E. Metzger, L.D. Grochowsky, Heat transfer between an impinging jet and a rotating disk, ASME J. Heat Transfer 99 (1977) 663–667.
[13] C.O. Popiel, L. Boguslowski, Local heat transfer from a rotating disk to an impinging round jet, ASME J. Heat Transfer 108 (1986) 357–364.
[14] M.-Y. Wen, K.-J. Jang, An impingement cooling on a flat surface by using circular jet with longitudinal swirling strips, Int. J. Heat Mass Transfer 46 (2003) 4657–4667.
[15] S.A. Striegl, T.E. Diller, An analysis of the effect of entrainment temperature on jet impingement heat transfer, ASME J. Heat Transfer 106 (1984) 804–810.
[16] B.R. Hollworth, L.R. Gero, Entrainment effects on impingement heat transfer. Part II: local heat transfer measurements, ASME J. Heat Transfer 107 (1985) 910–915.
[17] R.J. Goldstein, K.A. Sobolik, W.S. Seol, Effect of entrainment on the heat transfer to a heated circular air jet impinging on a flat surface, ASME J. Heat Transfer 112 (1990) 608–611.
[18] J.W. Baughn, T.E. Hechanova, X. Yan, An experimental study on entrainment effects on the heat transfer from a flat surface to a heated circular impinging jet, ASME J. Heat Transfer 113 (1991) 1023–1025.
[19] E.M. Sparrow, R.J. Goldstein, M.A. Rouf, Effect of nozzle surface separation distance on impingement heat transfer for a jet in a crossflow, ASME J. Heat Transfer 97 (1975) 528–533.
[20] R.J. Goldstein, A.I. Behbahani, Impingement of a circular jet with and without cross flow, Int. J. Heat Mass Transfer 25 (1982) 1377–1382.
[21] S.J. Kline, F.A. McClintock, Describing uncertainties in single sample experiments, Mech. Eng. 75 (1953) 3–8.
[22] D.J. Shlien, A.K.M.F. Hussain, Visualization of the large-scale motion of a plane jet, flow visualization, in: Proceedings of the 3rd International Symposium of Flow Visualization, 1983.
[23] C.-M. Ho, N. Nosseir, Dynamics of an impinging jet. Part 1. The feedback phenomenon, J. Fluid Mech. 105 (1981) 119–142.
[24] S. Ziada, Feedback control of globally unstable flows: impinging shear flows, J. Fluids Struct. 9 (1995) 907–923.